



## **A numerical investigation of curve squeal in the case of constant wheel/rail friction**

Downloaded from: <https://research.chalmers.se>, 2025-12-04 22:46 UTC

Citation for the original published paper (version of record):

Pieringer, A. (2014). A numerical investigation of curve squeal in the case of constant wheel/rail friction. *Journal of Sound and Vibration*, 333(18): 4295-4313.  
<http://dx.doi.org/10.1016/j.jsv.2014.04.024>

N.B. When citing this work, cite the original published paper.

# A numerical investigation of curve squeal in the case of constant wheel/rail friction

A. Pieringer<sup>\*</sup>

*Division of Applied Acoustics/CHARMEC, Chalmers University of Technology,  
41296 Göteborg, Sweden*

---

## Abstract

Curve squeal is commonly attributed to self-excited vibrations of the railway wheel, which arise due to a large lateral creepage of the wheel tyre on the top of the rail during curving. The phenomenon involves stick/slip oscillations in the wheel/rail contact and is therefore strongly dependent on the prevailing friction conditions. The mechanism causing the instability is, however, still a subject of controversial discussion. Most authors introduce the negative slope of the friction characteristic as source of the instability, while others have found that squeal can also occur in the case of constant friction due to the coupling between normal and tangential dynamics. As a contribution to this discussion, a detailed model for high-frequency wheel/rail interaction during curving is presented in this paper and evaluated in the case of constant friction. The interaction model is formulated in the time domain and includes the coupling between normal and tangential directions. Track and wheel are described as linear systems using pre-calculated impulse response functions that are derived from detailed finite element models. The non-linear, non-steady state contact model is based on an influence function method for the elastic half-space. Real measured wheel and rail profiles are used. Numerical results from the interaction model confirm that stick/slip oscillations occur also in the case of constant friction. The choice of the lateral creepage, the value of the friction coefficient and the lateral contact position on the wheel tread are seen to have a strong influence on the occurrence and amplitude of the stick/slip oscillations. The results from the interaction model are in good qualitative agreement with previously published findings on curve squeal.

*Key words:* curve squeal, wheel/rail interaction, time-domain, squeal mechanism, friction, stick/slip

---

---

<sup>\*</sup> Tel.: +46 31 772 2209; fax: +46 31 772 2212.

*Email address:* astrid.pieringer@chalmers.se (A. Pieringer).

## 1 Introduction

Curve squeal is a highly disturbing tonal sound generated by a railway vehicle negotiating a sharp curve. This type of noise is commonly attributed to self-excited vibrations of the railway wheel [1].

Since Rudd [2] in accordance with an earlier paper by Stappenbeck [3] discarded longitudinal creepage and flange rubbing as relevant causes for curve squeal, it is widely accepted that curve squeal arises from stick/slip behaviour due to lateral creepage of the wheel tyre on the top of the rail. The actual mechanism of the instability is however still a controversial topic. Rudd [2] introduced the negative slope of the friction characteristic (i.e. decreasing friction for increasing sliding velocity) as the source of the instability and most subsequent models have adopted this approach [4–11]. The existence of a ‘falling’ regime of the friction characteristic in wheel/rail contact is experimentally well substantiated, see e.g. [8,12–16]. As friction is however difficult to measure, it is inevitable to make assumptions about the exact shape of the friction characteristic in models for curve squeal. Correspondingly, many different friction curves have been used in the literature.

From a mathematical point of view, the instability can also be explained by the coupling between normal and tangential dynamics, leading to the non-symmetry of the system’s stiffness matrix [17]. This mechanism is exemplified by Hoffmann et al. [18] with a model having two degrees of freedom. Glocker et al. [19] recently presented a curve squeal model that shows stick/slip oscillations in the case of a constant friction coefficient. They identified one axial mode with zero nodal circles and two radial modes of the wheel, which occur at similar frequencies, as essential for the squeal mechanism. Simulation results showing stick/slip in the case of constant friction have also been reported by Ben Othman [20] and Brunel et al. [10]. Some experimental evidence that squeal occurs in the case of constant friction has been presented by Koch et al. [21], who performed measurements on a test rig. Also the conditions at some sites in the Australian railway network suggest the existence of an alternative squeal mechanism [22].

It is possible that both squeal mechanisms coexist in practice and this might be one reason why some models (for certain parameter combinations and initial conditions) show squeal in the case of a constant friction coefficient while others do not. Another reason is certainly that the results of all the models presented depend on model assumptions and the level of model complexity included. Curve squeal, which is an intrinsically non-linear and transient phenomenon, still poses a challenge in modelling. Frequency domain models can predict which modes are prone to squeal, but models aiming to predict squeal amplitudes have to be formulated in the time-domain. Due to the required computational effort of time-domain solutions, it is usually necessary to simplify wheel, rail and contact dynamics, and, by consequence, the models might

not include all the important features of the phenomenon.

As curve squeal is closely related to the excitation of wheel modes, most authors of time-domain models opt for a detailed wheel model. A modal model of the railway wheel or wheelset derived from a finite element (FE) model has e.g. been considered in the models [4,5,9,10,19,23]. The rail dynamics has, however, only been included in a few time-domain models [4,5,23]. Huang et al. [23] found that the simulation results change considerably if the rail is assumed to be rigid, while Périard [5] concluded that there was no significant influence of the rail dynamics on squeal during steady-state curving. The knowledge about the influence of different contact models on the simulation results is still fairly limited. Most models use analytical formulas to represent the creep force / creep relation, which can only partly represent the non-linear processes in the contact zone. Périard [5] included a modified version of Kalker's steady-state contact model FASTSIM [24] in his squeal model. To the knowledge of the authors, so far no transient, three-dimensional contact model has been used in a squeal model.

The aim of the work presented in this paper is to contribute to the modelling and understanding of curve squeal by proposing a detailed time-domain model for dynamic wheel/rail interaction that considers the coupling between normal and tangential directions. Thus, the model covers the generation of squeal noise in the wheel/rail contact, which is seen as the central problem in squeal prediction, but does not include sound radiation from the wheel. The computational effort in the wheel/rail interaction model is reduced by representing vehicle and track by impulse response functions derived from detailed FE models, which are calculated in advance. This technique, which has proven efficient for instance in the area of tyre/road noise [25] and in vertical wheel/rail interaction [26], makes it possible to include a three-dimensional, non-linear and transient contact model that is solved at each time step in the interaction model. This interaction model has shown stick/slip oscillations in combination with a velocity-dependent friction coefficient [27,28]. As a contribution to the discussion about the squeal mechanism, the work presented in this paper is limited to constant friction. After a description of the wheel/rail interaction model in Section 2, a parameter study is presented in Section 3 in order to investigate whether instabilities occur due to the coupling between normal and tangential dynamics.

## 2 Wheel/rail interaction model

The wheel/rail interaction model is primarily intended for quasi-static curving of the leading inner wheel in a railway bogie. The model relies on the wheel/rail contact position and the angle of attack of the wheelset (i.e. the lateral creepage) as given input parameters. These parameters can be pre-

calculated with a vehicle dynamics program.

Fig. 1 shows the reference frame of the wheel/rail interaction model. The  $x$ -direction (1-direction) is the rolling direction along the rail. The lateral direction is the  $y$ -direction (2-direction) pointing towards the field side of the wheel. The vertical (or normal)  $z$ -coordinate (3-coordinate) is pointing into the rail. This reference frame is moving with the nominal contact point along the rail.

The detailed FE models used for wheel and track include the longitudinal, lat-

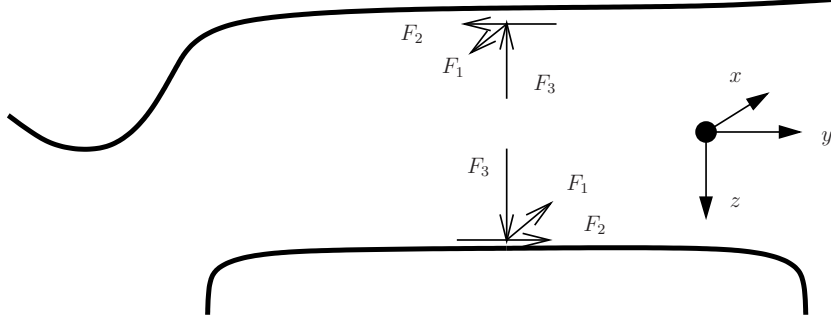


Fig. 1. Reference frame of the interaction model.

eral and vertical dynamics. Although all three directions could also be included in the wheel/rail interaction model, where wheel and track are represented by impulse response functions calculated from these FE models, the present study is limited to vertical and lateral dynamics of wheel and track. The wheel/rail contact is however treated as fully three-dimensional.

## 2.1 Wheel model

The vehicle is represented by a single flexible wheel, which is modelled by axisymmetric finite elements using a commercial finite element software. Fig. 2 shows the meshed cross-section of the selected wheel, which is a C20 metro wheel of diameter 780 mm. A rigid constraint is applied at the inner edge of the hub, where the wheel would be connected to the axle. The material data of the wheel are listed in Table 1.

With this FE model, the eigenfrequencies (see Table 2 and Fig. 3) and corresponding eigenmodes have been calculated up to 7 kHz. The eigenmodes are classified according to their predominant motion in axial, radial and circumferential modes, which have  $n$  nodal diameters and  $m$  nodal circles [1]. The axial modes will be denoted  $(n,m,a)$ . As  $m > 0$  does not occur for radial and circumferential modes in the frequency range of interest, they will be referred to as  $(n,r)$  and  $(n,c)$ , respectively. Examples of two axial modes and one radial

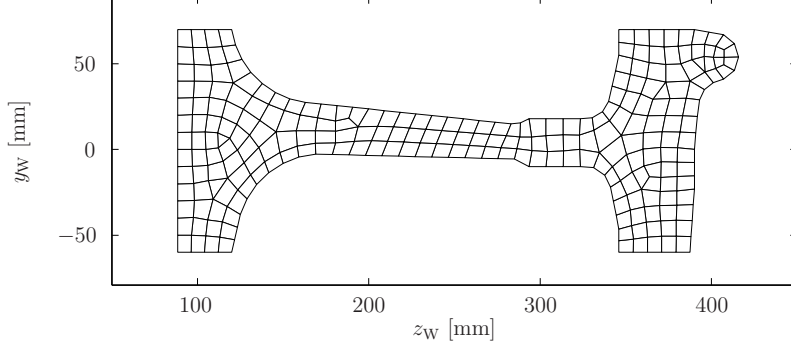


Fig. 2. FE mesh of the C20 wheel cross-section.

Table 1

Material properties of the wheel and the continuously supported rail

	Wheel	Rail	Pad
Young's modulus	207 GPa	207 GPa	4.8 MPa
Poisson's ratio	0.3	0.3	0.45
Density	7860 kg/m <sup>3</sup>	7860 kg/m <sup>3</sup>	10 kg/m <sup>3</sup>
Damping loss factor	see Eq. (1)	0.01	0.25

mode are shown in Fig. 4. The omission of the axle is known to lead to errors in eigenfrequency and mode shape for modes with  $n \leq 1$ , but has a negligible effect on higher-order modes [1]. As especially higher-order axial modes (with  $n \geq 2$ ) have been found to be important for curve squeal [1,9], this is not seen as critical for the investigation of squeal noise.

The eigenmodes are assigned a modal damping ratio  $\zeta$  using the approximate values proposed by Thompson [1]:

$$\zeta = \begin{cases} 10^{-3} & \text{for } n = 0 \\ 10^{-2} & \text{for } n = 1 \\ 10^{-4} & \text{for } n \geq 2 \end{cases} \quad (1)$$

The mode (1,r) is assigned a damping ratio of 1, since this mode appears too strongly in the frequency response function, when the influence of the axle is disregarded [1]. These damping ratios are used as a first approximation. Considering the importance of wheel damping for the occurrence of squeal, measured modal damping ratios should be used for the investigation of a specific squeal problem in a specific curve.

After determining the contact point on the wheel (see Section 2.3), the wheel receptances in the corresponding node are calculated by modal superposition. In addition to the modes of the flexible wheel calculated with the FE model,

Table 2

Eigenfrequencies  $f$  of the C20 wheel up to 7 kHz calculated with the FE model. The modes are classified according to mode type, number of nodal diameters  $n$  and number of nodal circles  $m$ .

<b>Axial modes</b>									
Zero nodal circles (m=0)									
n [-]	0	1	2	3	4	5	6	7	8
f [Hz]	332.8	243.2	429.9	1143	2058	3071	4131	5216	6316
One nodal circle (m=1)									
n [-]	0	1	2	3	4	5	6	7	
f [Hz]	1924	2089	2585	3193	3881	4635	5454	6343	
Two nodal circles (m=2)									
n [-]	0	1	2	3	4	5			
f [Hz]	4177	4237	4417	4872	5547	6406			
<b>Radial modes (m=0)</b>									
n [-]	0	1	2	3	4	5	6	7	
f [Hz]	3625	1586	2243	2834	3536	4350	5268	6269	
<b>Circumferential modes (m=0)</b>									
n [-]	0	1	2						
f [Hz]	722.0	3886	5228						

the rigid body modes of the complete wheelset including the primary suspension are considered. Notably translation in vertical direction (11.1 Hz), translation in lateral direction (14.4 Hz) and rotation in the vertical/lateral plane (16.5 Hz) are included in the modal summation. Fig. 5 shows as examples the vertical and lateral point receptances and the vertical/lateral cross-receptance for the node at  $y_W = -32$  mm on the wheel tread. This node corresponds to the nominal simulation case in Section 3.

The impulse response functions (or Green's functions) of the wheel,  $g_{ij}^W$ , are then obtained by inverse Fourier transform from the wheel receptances,  $G_{ij}^W$ :

$$g_{ij}^W(t) = \mathcal{F}^{-1} \left( G_{ij}^W(f) \right), \quad i, j = 2, 3. \quad (2)$$

The subscripts  $i$  and  $j$  denote the excitation and response directions, respectively. The first 0.4 s of the impulse response functions corresponding to the receptances from Fig. 5 are presented in Fig. 6. As the wheel is very lightly

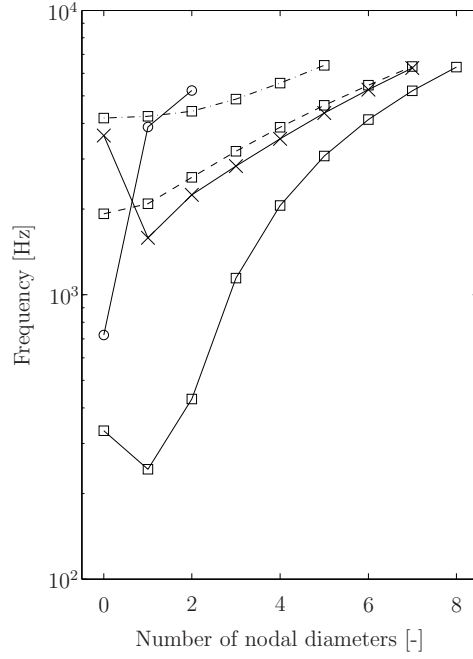


Fig. 3. Eigenfrequencies of the C20 wheel up to 7 kHz calculated with the FE model: axial modes ( $\square$ ), radial modes ( $\times$ ) and circumferential modes ( $\circ$ ) with zero nodal circles (—), one nodal circle (---) and two nodal circles (- · -).

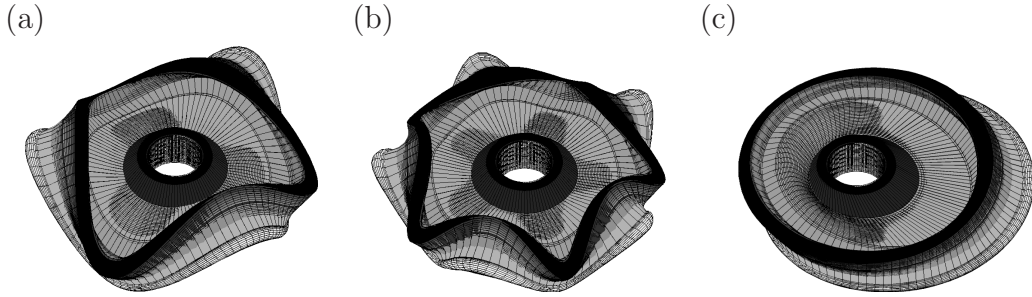


Fig. 4. Examples of wheel modes: (a) axial mode (3,0,a); (b) axial mode (5,0,a); (c) radial mode (1,r).

139 damped, the impulse responses decrease slowly and long signals have to be  
 140 considered. The total length of the impulse response signals taken into ac-  
 141 count is 20 s.

142 In the interaction model, the lateral and vertical displacements of the wheel at  
 143 the contact point,  $\xi_2^W(t)$  and  $\xi_3^W(t)$ , are calculated by convoluting the contact  
 144 forces  $F_2$  and  $F_3$  with the Green's functions

$$\xi_j^W(t) = - \int_0^t \sum_{i=2}^3 F_i(\tau) g_{ij}^W(t - \tau) d\tau, \quad j = 2, 3. \quad (3)$$



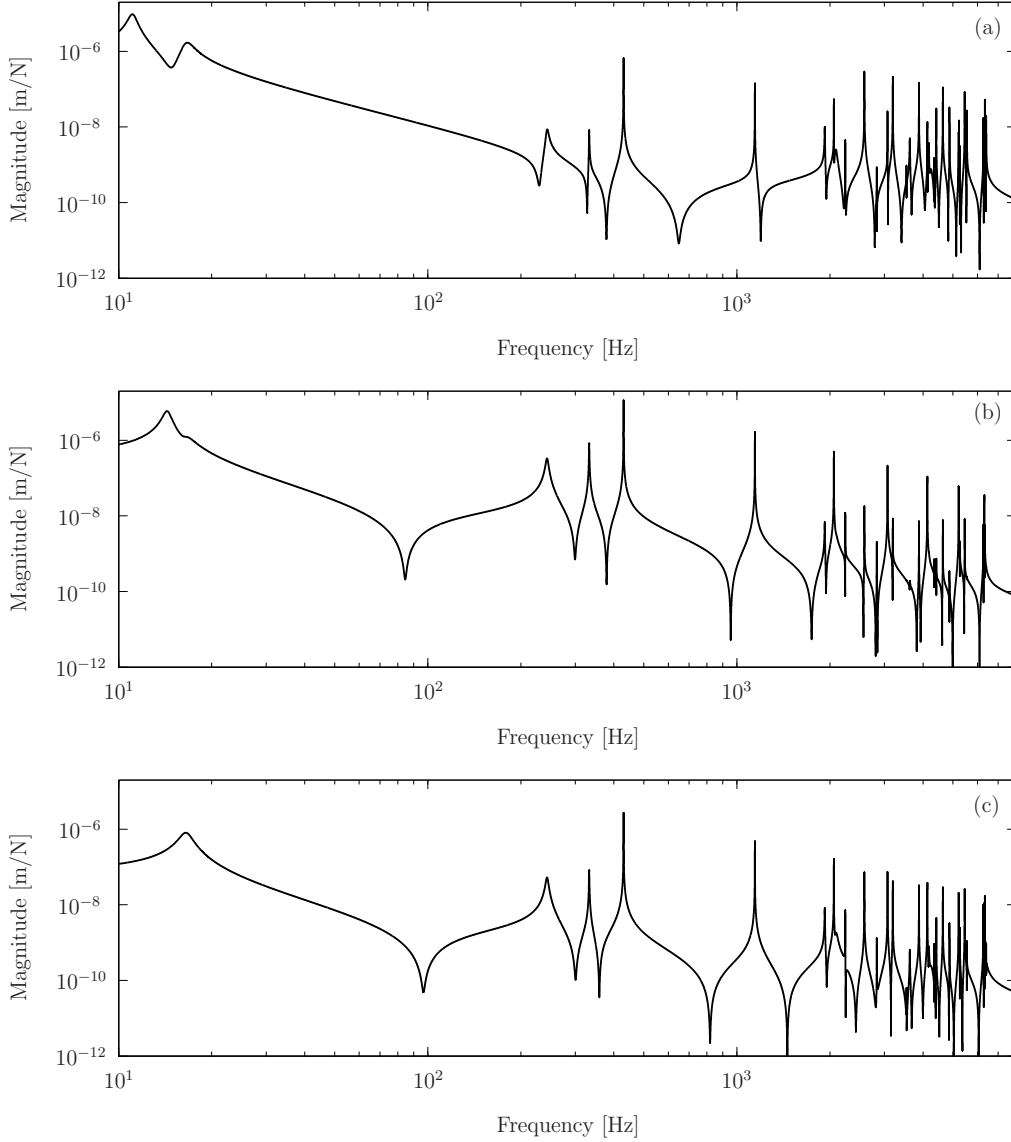


Fig. 5. Magnitudes of the wheel receptance at  $y_W = -32$  mm on the tread: (a) vertical point receptance, (b) lateral point receptance, (c) vertical/lateral cross receptance.

The influence of wheel rotation is neglected.

## 2.2 Track model

The track model consists of one continuously supported rail of type BV50 (a common Swedish rail type) and is built with waveguide finite elements using the software package WANDS [29]. This model takes advantage of the two-dimensional geometry of the rail having a constant cross-section in  $x$ -direction, but nonetheless considers the three-dimensional nature of the vibration by as-

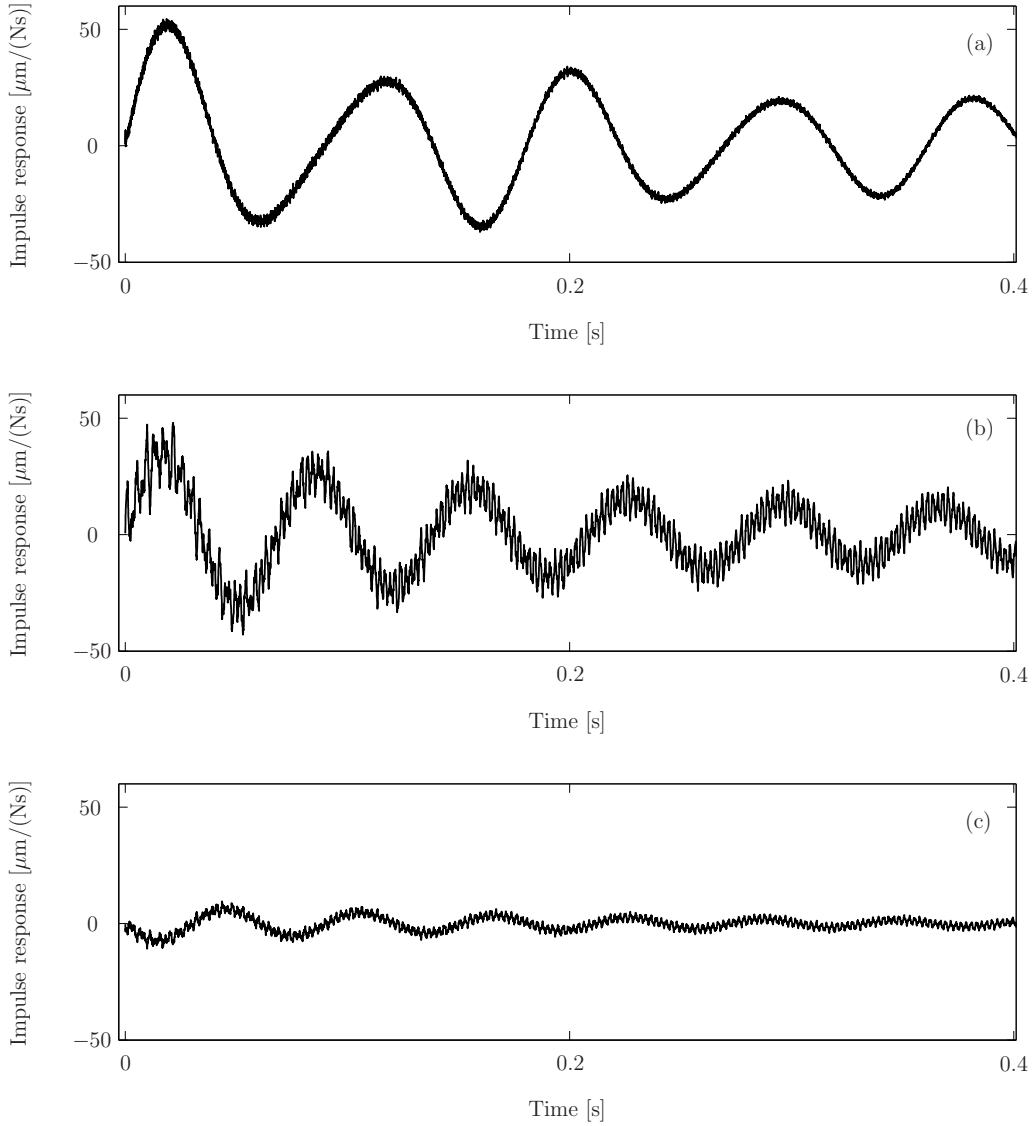


Fig. 6. Impulse response functions of the wheel calculated at  $y_W = -32$  mm on the tread : (a) vertical, (b) lateral, (c) vertical/lateral.

suming a wave-type solution along the rail. Cross-sectional deformations of the rail, which are important for high-frequency applications, are taken into account.

The waveguide finite element (WFE) mesh of the continuously supported rail, which consists of eight-noded isoparametric quadrilateral elements, is presented in Fig. 7. The material data of rail and support, which are chosen similar to the data given in [29], are listed in Table 1. The vertical stiffness of the continuous support corresponds to soft rail supports.

The equations of the WFE model are presented by Nilsson et al. in [29]. Only a short summary is given here.

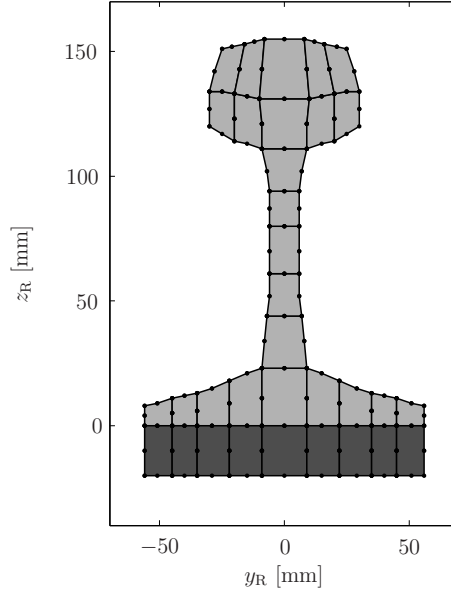


Fig. 7. WFE mesh of the BV50 rail.

The basic principle of the WFE method is that the displacement  $\mathbf{u} = [u_x, u_y, u_z]^T$  - in the  $x$ -,  $y$ - and  $z$ -directions - in one waveguide finite element is formulated as

$$\mathbf{u} = \mathbf{N}(y, z) \hat{\mathbf{u}}(x), \quad (4)$$

where  $\hat{\mathbf{u}}$  is the vector of nodal displacements and  $\mathbf{N}(y, z)$  are two-dimensional (2D) FE shape functions; i.e. a 2D mesh is sufficient to describe the three-dimensional structure.

In the same manner as for standard FE models, the complete WFE model is assembled from the formulation on element level. For free harmonic motion, the equations of the assembled WFE model represent an eigenvalue problem in wavenumber  $k$  at a given frequency  $\omega$ . The eigenvectors  $\tilde{\mathbf{U}}_n$  correspond to cross-sectional wave shapes. The eigenvalues  $k_n$  obtained as complex-valued wavenumbers describe propagation and decay of the waves along the rail. For an implicit time dependence  $e^{i\omega t}$ , the amplitude of a free harmonic wave propagating in the positive  $x$ -direction is thus described by

$$\hat{\mathbf{U}}_n(x) = \tilde{\mathbf{U}}_n e^{-ik_n x}, \quad (5)$$

where  $\hat{\mathbf{U}}_n$  is the global displacement vector containing all degrees of freedom in the cross-section. The eigenvalues are represented in Fig. 8 in the form of the dispersion relation. The wave shapes belonging to the different wave types in Fig. 8 are shown in Fig. 9 for the case  $k_n = 1$  rad/m.

The response to forced excitation is obtained by superposing the contributions from the different waves. For propagation in the positive  $x$ -direction, the global displacement vector  $\hat{\mathbf{U}}_0$  obtained due to a harmonic point force at  $x = 0$

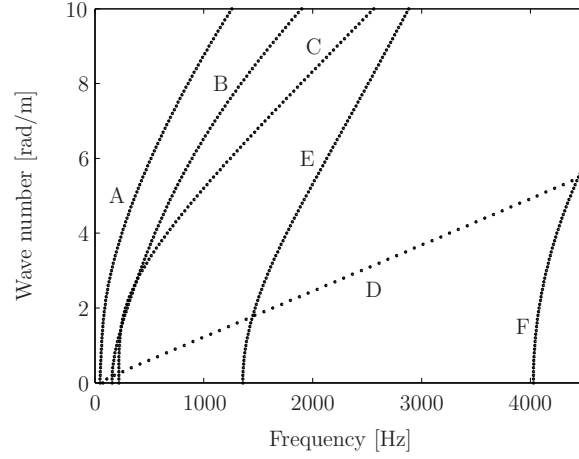


Fig. 8. Dispersion relation for the continuously supported rail. Wave types: (A) Lateral bending wave, (B) Vertical bending wave, (C) Torsional wave, (D) Longitudinal wave, (E) Web bending wave 1, (F) Web bending wave 2.

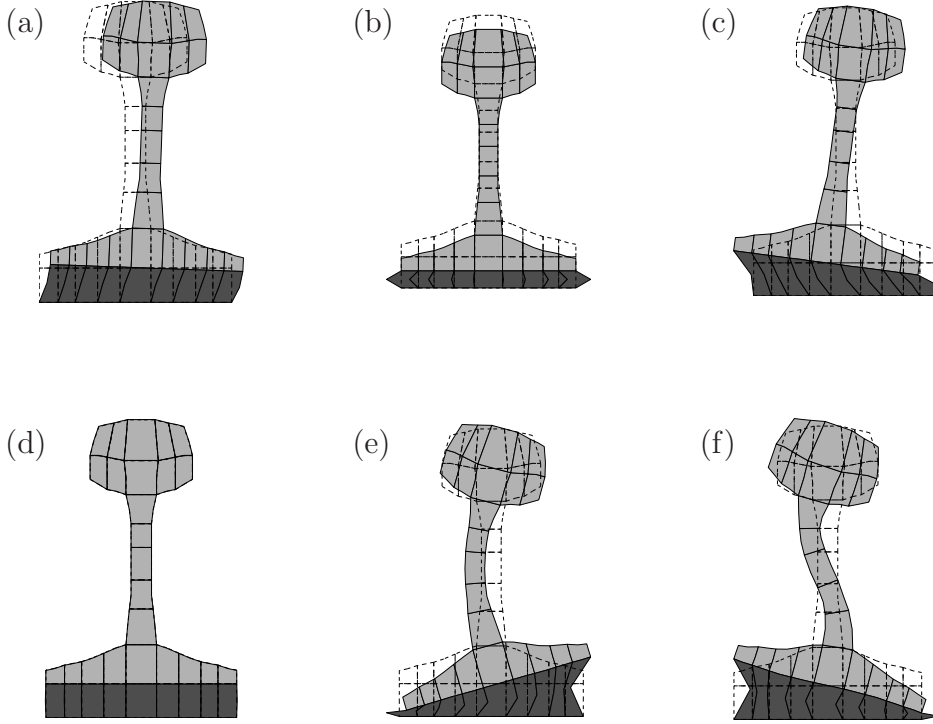


Fig. 9. Wave shapes at  $k_n = 1$  rad/m: (a) Lateral bending wave, (b) Vertical bending wave, (c) Torsional wave, (d) Longitudinal wave, (e) Web bending wave 1, (f) Web bending wave 2.

183 reads [29]

$$\hat{\mathbf{U}}_0(x) = \sum_n A_n(\tilde{\mathbf{F}}_0) \tilde{\mathbf{U}}_n e^{-ik_n x}, \quad (6)$$

where the force vector  $\tilde{\mathbf{F}}_0$  is formulated in the wavenumber domain. The expression for the amplitudes  $A_n(\tilde{\mathbf{F}}_0)$  is given in [29].

For the predetermined lateral contact position on the rail (see Section 2.3), receptances are calculated from the result of Equation (6). Fig. 10 shows as examples the vertical and lateral point receptances and the vertical/lateral cross-receptance for the node at  $y_R = 12$  mm on the rail head. This node corresponds to the nominal simulation case in Section 3.

In the interaction model, the track is represented by a special type of Green's functions denoted moving Green's functions,  $g_{ij,v}^{R,x_0}(t)$ , which include the motion of the nominal contact point along the rail [28,30]. The function  $g_{ij,v}^{R,x_0}(t)$  describes, for excitation of the rail (index R) in  $i$ -direction at the position  $x_0$  at time  $t_0 = 0$ , the displacement response of the rail in  $j$ -direction at a point moving with train speed  $v$  away from the excitation, thus at the nominal contact point between wheel and rail. The discrete version of the moving Green's function  $g_{ij,v}^{R,x_0}(t)$  is constructed from (ordinary) Green's functions  $g_{ij}^{R,x_0,x_0+\alpha}(t)$ , where the superscripts specify the excitation point  $x_0$  and the response point  $x_0 + \alpha$  on the rail. The Green's functions  $g_{ij}^{R,x_0,x_0+\alpha}(t)$  are obtained from the corresponding track transfer receptances by inverse Fourier transform:

$$g_{ij}^{R,x_0,x_0+\alpha}(t) = \mathcal{F}^{-1} \left( G_{ij}^{R,x_0,x_0+\alpha}(f) \right), \quad i, j = 2, 3. \quad (7)$$

The lateral and vertical displacements of the track at the contact point,  $\xi_2^R(t)$  and  $\xi_3^R(t)$ , are calculated by convoluting the contact forces with the moving Green's functions

$$\xi_j^R(t) = \int_0^t \sum_{i=2}^3 F_i(\tau) g_{v,ij}^{R,v\tau}(t - \tau) d\tau, \quad j = 2, 3. \quad (8)$$

In the case of the continuously supported track used in this article, the moving Green's functions are independent of the excitation position  $x_0$  on the rail. Fig. 11 shows as example the moving Green's functions of the track obtained for excitation at the lateral contact position  $y_R = 12$  mm and a train speed  $v = 50$  km/h. As the track is a waveguide and has in addition much higher damping than the wheel, it is well characterised by considerably shorter Green's functions than the wheel. The total length of the moving Green's functions taken into account is 0.25 s.

### 2.3 Contact position on wheel and rail

Measured wheel and rail profiles are used in the wheel/rail interaction model. The wheel profile is a S1002 profile worn over 169 000 km. The rail profile is a

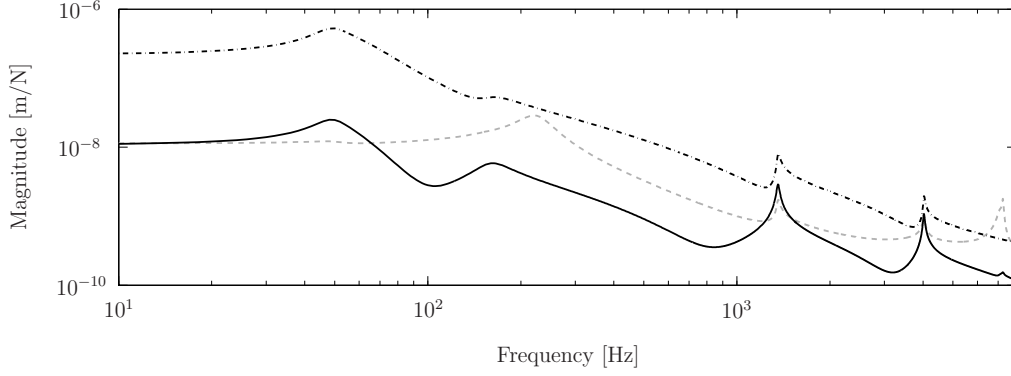


Fig. 10. Magnitudes of the track receptance at the rail head at  $y_R = 12$  mm : --- (grey) vertical point receptance, - · - lateral point receptance, — vertical/lateral cross-receptance.

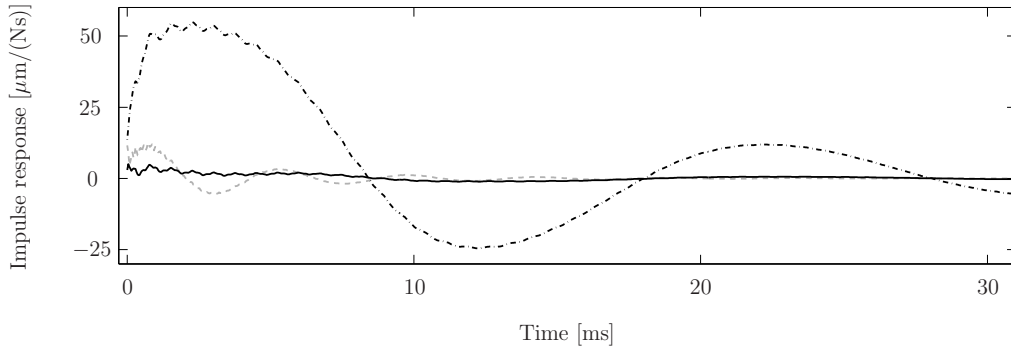


Fig. 11. Moving Green's functions of the track calculated for a lateral contact position on the rail  $y_R = 12$  mm and a train speed  $v = 50$  km/h: --- (grey) vertical, - · - lateral, — vertical/lateral.

218 BV50 profile with inclination 1:40 measured at a curve in the network of Stock-  
 219 holm metro, where severe corrugation and squeal occur [31]. For these profiles,  
 220 the contact points on wheel and rail have been determined as a function of  
 221 the relative lateral displacement  $\Delta y^{WR}$  of the wheelset on the rail, with a pre-  
 222 processor of the commercial vehicle-track interaction software GENSYs [32].  
 223 The roll angle of the wheelset and the deflection of the primary wheelset sus-  
 224 pension for a chosen vertical preload  $P$  of 65 kN have been taken into account.  
 225 Fig. 12 shows the results for the inner rail, which are used in the interaction  
 226 model. For a given lateral displacement  $\Delta y^{WR}$ , the actual profiles around the  
 227 contact point on wheel and rail are considered in the algorithm. The wheel  
 228 and track receptances calculated in the node closest to the contact point are  
 229 used. The wheel and track receptances presented as examples in Sections 2.1  
 230 and 2.2 correspond to a relative lateral displacement of the wheelset on the  
 231 rail of  $-15$  mm.

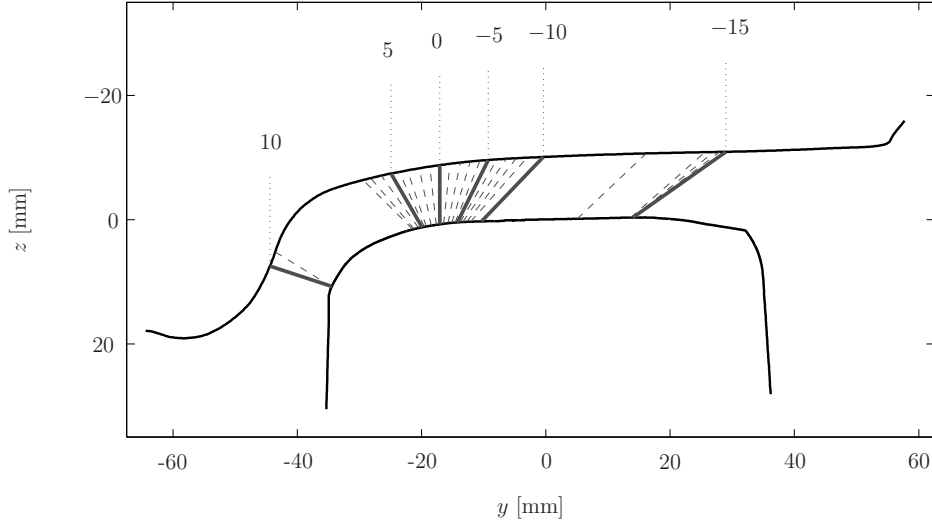


Fig. 12. Contact points for a worn wheel profile S1002 on a worn rail profile BV50 with inclination 1:40 calculated for different lateral displacements  $\Delta y^{\text{WR}}$  [mm] of the wheelset on the rail; results given for 1 mm steps.

#### 2.4 Normal contact model

The contact model is an implementation of Kalker's model CONTACT [33], which is a three-dimensional, non-steady state rolling contact model based on the assumption that wheel and rail can be locally approximated by elastic half-spaces. In addition to the parameters included in CONTACT, the contact model used in this article considers the combined roughness of wheel and rail on several parallel lines in the rolling direction and the contribution of the structural dynamics of wheel and rail to the creepage.

A potential contact area is introduced and divided into  $N$  rectangular elements with side lengths  $\Delta x$  and  $\Delta y$  in  $x$ - and  $y$ -directions, respectively. Assuming that wheel and rail are made of the same material, quasi-identity holds and, consequently, the normal and tangential contact problems can be solved separately [33].

The normal contact problem consists in determining which elements of the potential contact area are in contact, and calculating the local vertical displacement  $u_{I3}$  and the contact pressure  $p_{I3}$  in every element  $I$ .

The local vertical displacement, which is the displacement difference between rail and wheel,

$$u_{I3} = u_{I3}^{\text{R}} - u_{I3}^{\text{W}}, \quad I = 1, \dots, N, \quad (9)$$

250 is related to the contact pressure according to

$$u_{I3} = \sum_{J=1}^N A_{I3J3} p_{J3}, \quad I = 1, \dots, N, \quad (10)$$

251 where  $A_{I3J3}$  are influence coefficients for the elastic half-space, e.g. found  
 252 in [33]. The total vertical contact force,  $F_3$ , is obtained by summing the con-  
 253 tributions from the different elements:

$$F_3 = \sum_{I=1}^N p_{I3} \Delta x \Delta y. \quad (11)$$

254 Introducing the variable  $d_I$  describing the distance between the deformed bod-  
 255 ies in each element, the contact conditions are formulated as

$$\begin{aligned} d_I &\geq 0 \\ p_{I3} &\geq 0 \\ d_I p_{I3} &= 0 \end{aligned} \quad (12)$$

256 If contact occurs in a surface element, the distance is zero and the contact  
 257 pressure is positive. If contact does not occur, the distance is positive and  
 258 the pressure is zero. Adhesion and penetration are excluded by Equation (12).  
 259 The distance  $d_I$  is obtained as

$$d_I = -\delta + u_{I3} + z_I^R - z_I^W + r_I^R - r_I^W, \quad (13)$$

260 where  $z_I^R$  and  $z_I^W$  are the profiles of rail and wheel,  $r_I^R$  and  $r_I^W$  are the roughness  
 261 of rail and wheel, and  $\delta$  is the approach of distant points

$$\delta = \xi_3^W - \xi_3^R. \quad (14)$$

262 The normal contact problem is solved with an active set algorithm [33].

## 263 2.5 Tangential contact model

264 In frictional rolling contact, the contact area is divided into a stick and a slip  
 265 area. The tangential contact problem consists in determining which elements  
 266 are in stick and in slip, and calculating the local tangential displacements  $u_{I\tau}$   
 and tangential stresses  $p_{I\tau}$  at the surface.

267 The relation between local tangential displacements and tangential stresses is  
 268 given by  
 269

$$u_{I\tau} = \sum_{\alpha=1}^2 \sum_{J=1}^N A_{I\tau J\alpha} p_{J\alpha}, \quad \tau = 1, 2, \quad (15)$$



where  $A_{I\tau J\alpha}$  are influence coefficients for the elastic half-space, e.g. found in [33]. The tangential forces,  $F_\tau$ , are obtained by summing the contributions from the different elements:

$$F_\tau = \sum_{I=1}^N p_{I\tau} \Delta x \Delta y, \quad \tau = 1, 2. \quad (16)$$

A contact element belongs to the stick area if the local shift,  $S_{I\tau}$ , vanishes:

$$S_{I\tau} = 0, \quad \tau = 1, 2. \quad (17)$$

Otherwise the contact element belongs to the slip area. The local shift, defined as the relative displacement of two opposing particles of the wheel and the rail with respect to each other in one time step  $\Delta t = \Delta x/v$ , is obtained as

$$S_{I\tau} = u_{I\tau} + W_\tau^* - u'_{I\tau}, \quad \tau = 1, 2. \quad (18)$$

The variable  $u'_{I\tau}$  represents the local displacement at the previous time step. In Kalker's formulation,  $W_{I\tau}$  is the rigid shift calculated as

$$W_{I1} = (\xi - y\phi) \Delta x \quad (19)$$

$$W_{I2} = (\eta + x\phi) \Delta x, \quad (20)$$

where  $\xi$ ,  $\eta$  and  $\phi$  are the longitudinal, lateral and spin creepages. In this paper, the contribution of the structural dynamics of wheel and track is added to the rigid shift:

$$W_{I1}^* = W_{I1} \quad (21)$$

$$W_{I2}^* = W_{I2} + (\xi_2^R - \xi_2^W) - (\xi_2'^R - \xi_2'^W), \quad (22)$$

where  $\xi_2^R$  and  $\xi_2^W$  are the lateral displacements of rail and wheel at the previous time step.

In the slip area, the following relations hold:

$$\frac{p_{I\tau}}{\sqrt{p_{I1}^2 + p_{I2}^2}} = -\frac{S_{I\tau}}{\sqrt{S_{I1}^2 + S_{I2}^2}}, \quad \tau = 1, 2 \quad (23)$$

$$p_{I1}^2 + p_{I2}^2 = (\mu p_{I3})^2, \quad (24)$$

where  $\mu$  is the friction coefficient, which is assumed constant. Equation (23) ensures that the slip occurs in the direction opposite to the tangential stress. Equation (24) states that the tangential stress in the slip zone is equal to the traction bound  $\mu p_{I3}$ .

The tangential contact problem is solved with an active set algorithm [33] combined with the Newton-Raphson method.

### 291 3 Simulation results

292 In this section, the model described in Section 2 is applied to calculate high-  
 293 frequency wheel/rail interaction during curving. First, the model is verified  
 294 for quasi-static conditions. Second, dynamic calculations taking into account  
 295 the wheel and track dynamics are carried out for different parameter combi-  
 296 nations. If not stated differently in the text, the nominal parameters listed in  
 297 Table 3 are used in the simulations. Given the coordinate system and the sign  
 298 conventions used here, a negative value of the lateral creepage corresponds to  
 299 an underradial position of the wheelset in the curve, which is a typical config-  
 300 uration for the leading wheelset of the bogie [34]. In an underradial position,  
 301 the wheelset runs towards the outside of the curve with an angle of attack  
 302  $\alpha > 0$ . This situation is illustrated in Fig. 13. The contrary case with  $\alpha < 0$   
 303 is called overradial position and corresponds to a positive value of the lateral  
 304 creepage in the model. All simulations presented in this paper have been car-  
 305 ried out for smooth wheel and rail surfaces. The inclination of the contact  
 306 plane with regard to the horizontal plane has been neglected. Although the  
 307 contact angle is small for the contact positions on the wheel tread/rail head, it  
 308 should be noted that this simplification could influence the simulation results.  
 Wheel flange/rail gauge corner contact has not been considered.

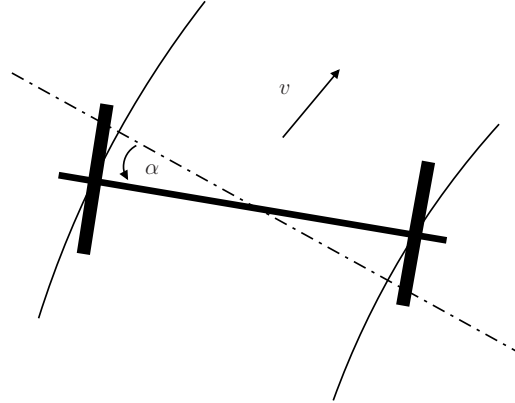


Fig. 13. Underradial position of the wheelset with angle of attack  $\alpha > 0$ .

#### 310 3.1 Verification of the contact model against CONTACT

311 Setting the wheel and track Green's functions to zero, i.e. assuming quasi-  
 312 static conditions, makes it possible to verify the interaction model against  
 313 Kalker's own implementation CONTACT of his variational theory of rolling  
 314 contact [33,35]. As both models are implementations of the same theory, very  
 315 similar results are expected. Differences can arise from the different solvers

Table 3

Nominal simulation parameters

Train speed	$v = 50 \text{ km/h}$
Lateral displacement of wheel on rail	$\Delta y^{\text{WR}} = -15 \text{ mm}$
Vertical static preload	$P = 65 \text{ kN}$
Longitudinal creepage	$\xi = 0$
Lateral creepage	$\eta = -1\%$
Spin creepage	$\phi = 0$
Friction coefficient	$\mu = 0.3$
Element length in $x$ -direction	$\Delta x = 0.5 \text{ mm}$
Element length in $y$ -direction	$\Delta y = 1 \text{ mm}$
Time step	$\Delta t = 36 \mu\text{s}$

316 used for the non-linear problem occurring in the tangential contact problem.  
 317 CONTACT uses a specially designed Gauss-Seidel type solver [36], while a  
 318 Newton-Raphson method is used in the present implementation. Furthermore,  
 319 different tolerances and round-off practices can lead to slightly different results.  
 320 Fig. 14 shows the division of the contact area into stick and slip zones obtained  
 321 with both models using the parameters from Table 3 and an imposed lateral  
 creepage of  $\eta = -0.2\%$ . Rolling direction is the positive  $x$ -direction. Both

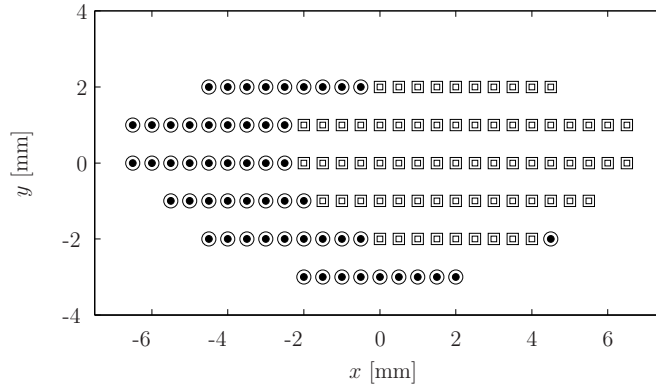


Fig. 14. Division of the contact zone: quasi-static case,  $\eta = -0.2\%$ . Stick zone:  
 □ CONTACT, □ interaction model; Slip zone: ○ CONTACT, ● interaction model.

322  
 323 models give identical divisions of the contact zone. Wheel and track particles  
 324 enter the contact zone at the leading edge and traverse the stick zone, before  
 325 they reach the slip zone at the trailing edge of the contact. The corresponding  
 326 distributions of the contact pressure and the total tangential stress are pre-  
 327 sented in Fig. 15. The tangential stress increases continuously from zero at the

328 leading edge towards the slip zone, where it reaches the traction bound  $\mu p_3$ .  
 The comparison of tangential stress and contact pressure obtained with both

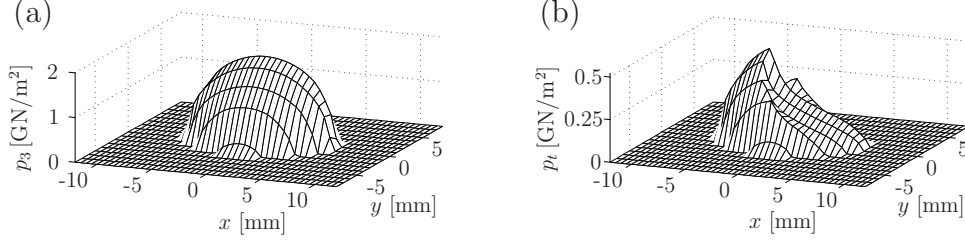


Fig. 15. Distribution of (a) contact pressure  $p_3$  and (b) total tangential stress  $p_t = \sqrt{p_1^2 + p_2^2}$  in the contact zone: quasi-static case,  $\eta = -0.2\%$ .

329 models on two selected lateral lines (Fig. 16) shows that the interaction model  
 330 is in very good agreement with CONTACT. The relative difference between  
 331 the stress distributions obtained does not exceed 0.75%.

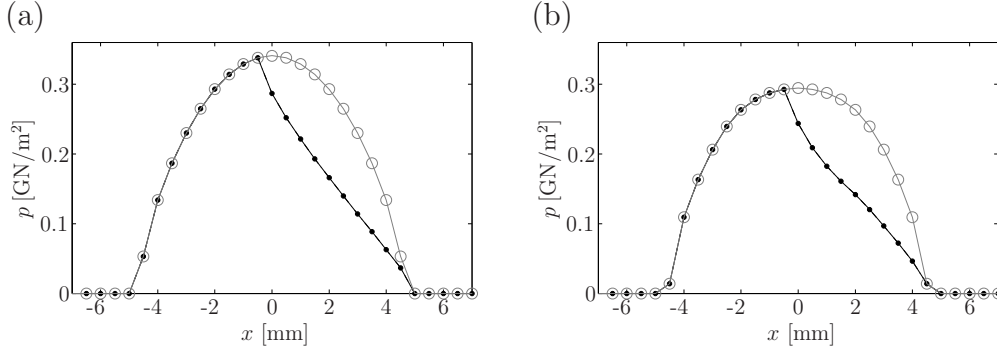


Fig. 16. Tangential stress  $p_t$  (in black) and traction bound  $\mu p_3$  (in grey) obtained with the interaction model (—) in comparison to CONTACT ( $\bullet$  /  $\circ$ ) for the quasi-static case,  $\eta = -0.2\%$ : (a) on line  $y = 2$  mm, (b) on line  $y = -2$  mm.

332

### 333 3.2 Dynamic wheel/rail interaction

334 The dynamic wheel/rail interaction during curving has been calculated for a  
 335 range of different input parameters in order to investigate possible instabilities.  
 336 In each simulation, the total simulated time is 3.5 s. The preload and the  
 creepages are applied gradually in the first 0.14 s of the simulation.

337 The time-domain simulations make it possible to determine the amplitude of  
 338 occurring stick/slip oscillations. A problem is, however, that only a finite time  
 339 interval is analysed and stick/slip oscillations that need a long time to build  
 340 up are difficult to detect. Against this background, a measure  $L_{F_2}$  based on  
 341 the rms-value of the lateral contact force signal is introduced to characterise  
 342

the relative instability of the simulations:

$$L_{F_2} = 20 \log \frac{F_{2,\text{rms}}}{1 \text{ N}}. \quad (25)$$

The rms-value  $F_{2,\text{rms}}$  of the transient part of the signal in a time period  $T$  is obtained as

$$F_{2,\text{rms}} = \sqrt{\frac{1}{T} \int_{t_1}^{t_1+T} (F_2(t) - \bar{F}_2)^2 dt}, \quad (26)$$

where  $\bar{F}_2$  is the mean value of the force in the considered time interval. The rms-value is calculated from the last 0.15 s of the force signal, and only frequency components above 150 Hz are considered in order to exclude contributions from the wheel suspension. As the mean value is subtracted from the force signal, cases with no stick/slip, where the force approaches a constant value, give low values of  $L_{F_2}$ . Although sound radiation from the wheel has not been calculated, the measure  $L_{F_2}$  based on the lateral contact force is also a good indicator for the likelihood of squeal to develop, - and to a certain degree - is an estimator for the strength of squeal.

In the simulation with the nominal parameters from Table 3, denoted simulation I, a pronounced stick/slip oscillation builds up. Fig. 17 presents the time series of the lateral contact force and Fig. 18 the corresponding power spectrum. The main frequency component in the spectrum (which, like all spectra presented in Section 3, has a frequency resolution of 6.8 Hz) is identified as 434 Hz, which is very close to the eigenfrequency of the (2,0,a) mode of the wheel at 430 Hz. Furthermore, the spectrum contains higher harmonics of this frequency. The measure  $L_{F_2}$  according to Equation (25) is 47.0 dB. Details of the stick/slip cycle are depicted in Figs. 19 and 20. During most of the cycle, the contact area is in full slip and the lateral contact force  $F_2$  coincides with the traction limit  $\mu F_3$ . Only during a short phase in each cycle, partial stick occurs at the leading edge of the contact zone, see Fig. 20(b) and (c), and the lateral force takes a value below the traction bound.

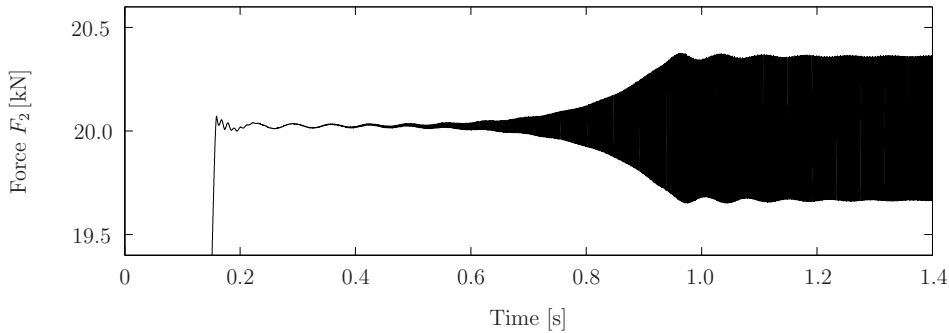


Fig. 17. Simulation I: time series of the lateral contact force  $F_2$ .

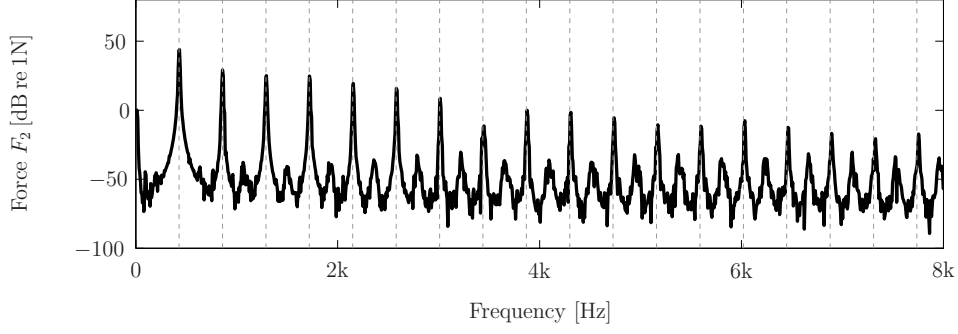


Fig. 18. Simulation I: power spectrum of the lateral contact force  $F_2$ . Multiples of the main frequency component at 434 Hz are indicated by vertical dashed lines.

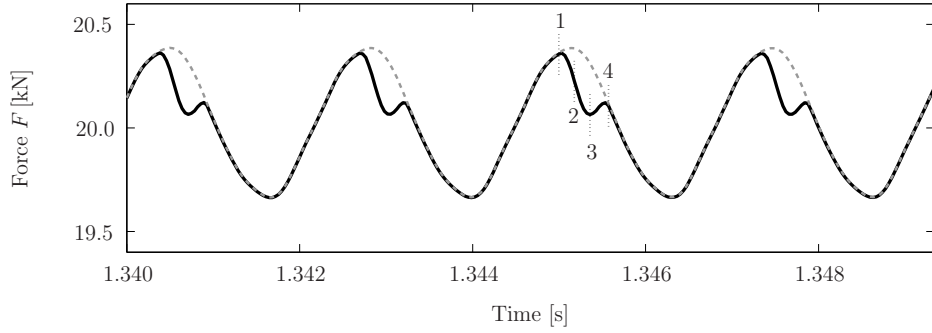


Fig. 19. Simulation I: zoom on time series of the contact forces; — lateral force  $F_2$ , - - - (grey) traction bound  $\mu F_3$ . The division of the contact zone at the time steps marked with Arabic numerals is depicted in Fig. 20.

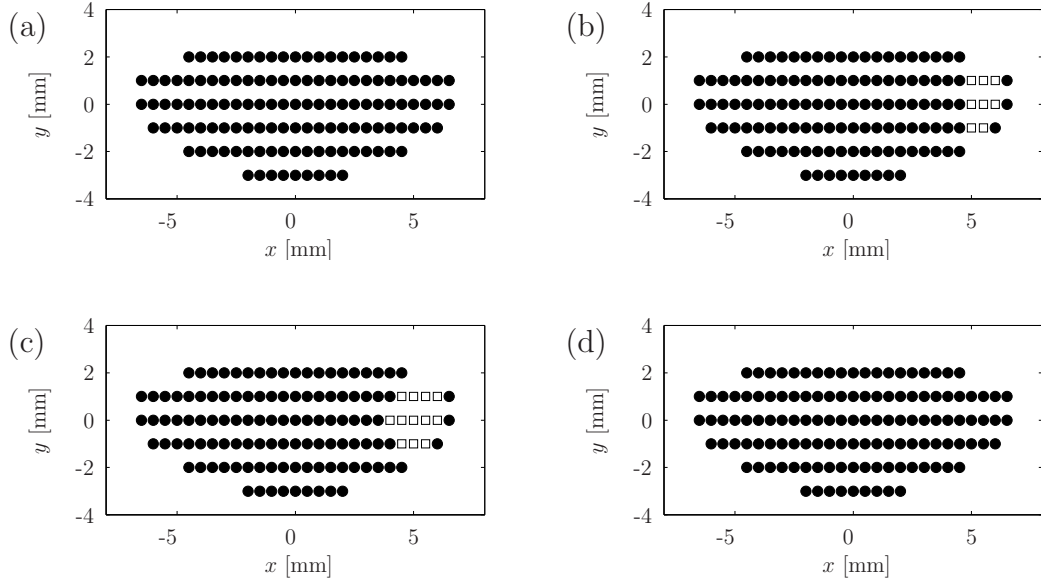


Fig. 20. Simulation I: division of contact zone in stick ( $\square$ ) and slip ( $\bullet$ ) zones in the time steps marked in Fig. 19; (a) step 1, (b) step 2, (c) step 3, (d) step 4.

### 3.2.1 Influence of lateral creepage and friction coefficient

The dynamic simulation I has been repeated for different values of lateral creepage and friction coefficient. The results are presented in Fig. 21 in terms of the measure  $L_{F_2}$  calculated from the lateral force signal. Both parameters, the imposed lateral creepage and the friction coefficient, are seen to have a strong influence on the occurrence and amplitudes of stick/slip oscillations. High levels  $L_{F_2}$  are only observed on the left side of Fig. 21 corresponding to negative values of the lateral creepage (i.e. underradial position of the wheelset in the curve). Another observation from Fig. 21 is that small changes in the parameters can lead to a sudden appearance (or disappearance) of pronounced stick/slip oscillations.

Simulations with  $L_{F_2} > 0$  dB, which have been denoted by Roman numerals in

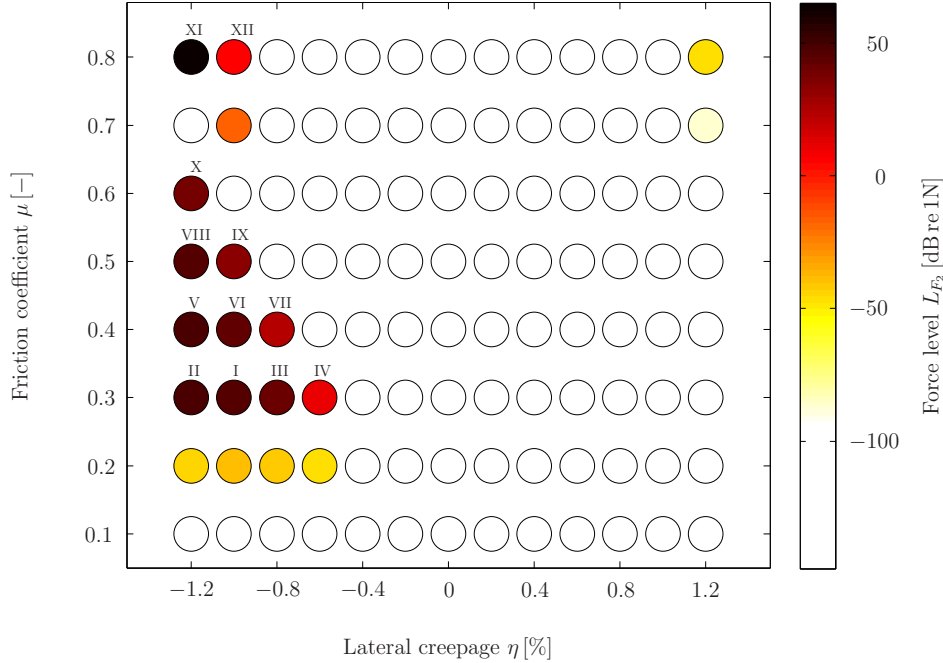


Fig. 21. Results of the dynamic simulations as function of the imposed lateral creepage  $\eta$  and the friction coefficient  $\mu$ : force level  $L_{F_2}$  calculated according to Equation (25); simulations with  $L_{F_2} > 0$  dB are denoted by Roman numerals.

Fig. 21, have been analysed in more detail. Among those, two groups can be identified according to the main frequency component; see the first two rows in Table 4. A third stick/slip frequency is found, when changing the lateral contact position; see Section 3.2.2 and Table 4. In the first group, which comprises simulations I-X, the main frequency component occurs at 434 Hz, which corresponds to the (2,0,a) mode of the wheel. This group has already been exemplified by the results of simulation I in Figs. 17 to 20. The second group consists of simulations XI and XII, where stick/slip develops at a frequency of

5235 Hz. This frequency is close to the eigenfrequencies of the (7,0,a) and (2,c) modes of the wheel, which are 5216 Hz and 5228 Hz, respectively. This second group of simulations is exemplified by the results from simulation XI presented in Figs. 22 to Fig. 25. The time signal of the lateral contact force (Fig. 22) reveals that the build-up of the stick/slip oscillation takes about three times as long as in the case of simulation I (Fig. 17). The change of mean value of the lateral force in Fig. 22 is explained by a lateral shift of the wheel on the rail. In the stick/slip oscillation of simulation XI, the lateral force stays below the traction limit  $\mu F_3$  at all times (Fig. 24) and the division of the contact zone oscillates between the two extremes depicted in Fig. 25.

Table 4

Main frequency component in simulations with  $L_{F_2} > 0$  dB.

Frequency [Hz]	Closest wheel modes	Simulations
434	(2,0,a)	I-X, XIV
5235	(7,0,a), (2,c)	XI, XII
1146	(3,0,a)	XIII

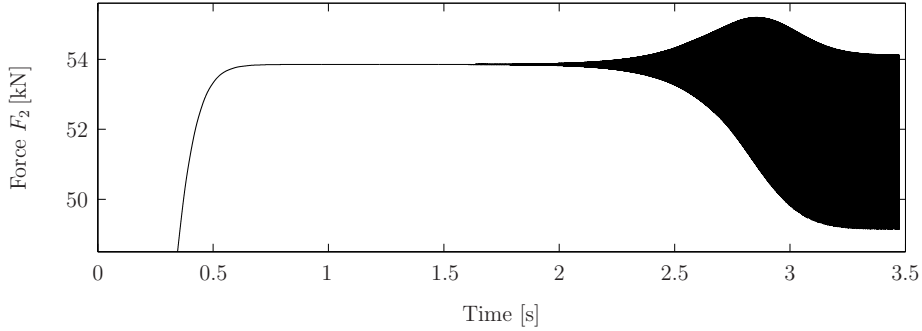


Fig. 22. Simulation XI: time series of the lateral contact force  $F_2$ .

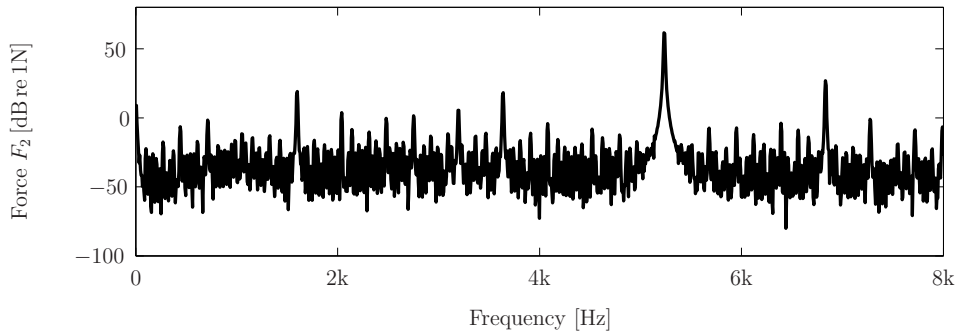


Fig. 23. Simulation XI: power spectrum of the lateral contact force  $F_2$ .



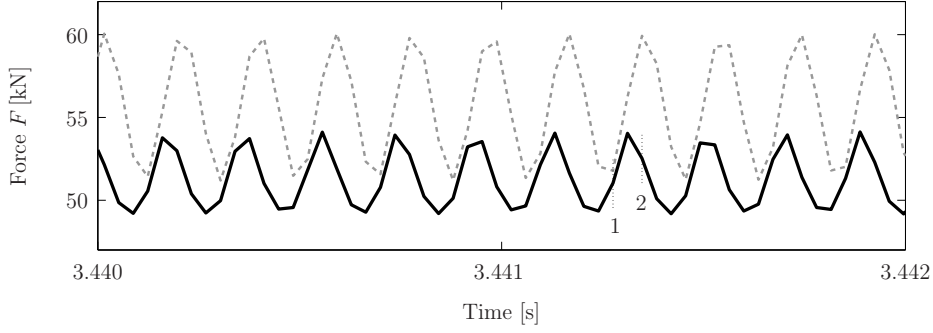


Fig. 24. Simulation XI: zoom on time series of the contact forces; — lateral force  $F_2$ , - - - (grey) traction bound  $\mu F_3$ . The division of the contact zone at the time steps marked with Arabic numerals is depicted in Fig. 25.

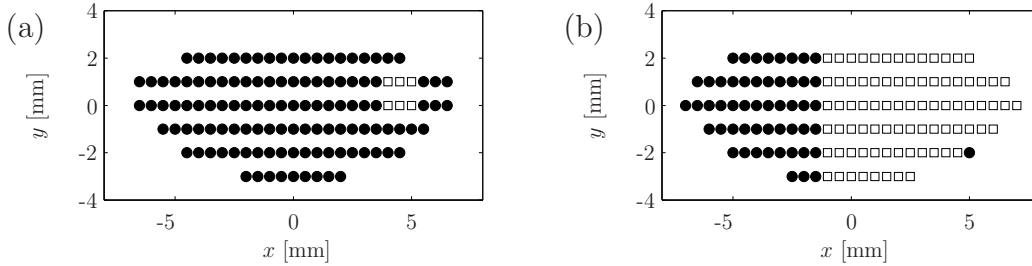


Fig. 25. Simulation XI: division of contact zone in stick ( $\square$ ) and slip ( $\bullet$ ) zones; (a) minimum size of the stick zone (corresponding to time step 1 in Fig. 24) and (b) maximum size of the stick zone (corresponding to time step 2 in Fig. 24).

### 3.2.2 Influence of the lateral contact position

Simulation I has also been repeated for four different values of the relative lateral displacement  $\Delta y^{\text{WR}}$  of the wheel on the rail (Fig. 26). In addition to simulation I, where  $\Delta y^{\text{WR}}$  is  $-15$  mm, pronounced stick/slip oscillations occur also for  $-10$  mm (simulation XIII) and  $-5$  mm (simulation XIV), but not for  $0$  mm and  $5$  mm, where the contact on the wheel tread occurs more towards the wheel flange (Fig. 12).

Simulation XIV belongs to the group of simulations with a main frequency component at  $434$  Hz, while the stick/slip oscillation in simulation XIII occurs at  $1146$  Hz, which corresponds to the (3,0,a) mode of the wheel at  $1143$  Hz. The results of simulation XIII are presented in Figs. 27 to 30. The stick/slip oscillation (Fig. 27) develops twice as fast as compared to simulation I (Fig. 17), and interacts initially with the initial oscillations of the wheel suspension. The first few higher harmonics in the power spectrum of the lateral contact force (Fig. 28) have similar magnitudes to the fundamental tone at  $1146$  Hz. This

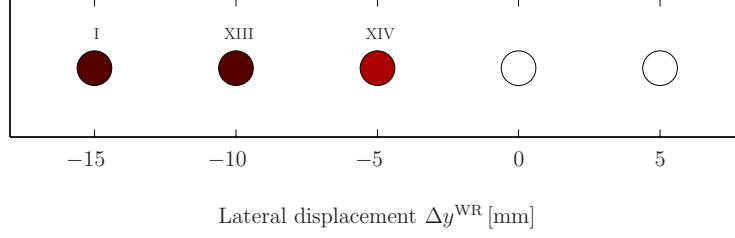


Fig. 26. Results of the dynamic simulations as function of the relative lateral displacement  $\Delta y^{\text{WR}}$  of the wheel on the rail: force level  $L_{F_2}$  according to Equation (25); simulations with  $L_{F_2} > 0$  dB are denoted by Roman numerals. Colour bar as in Fig. 21.

413 highlights the strongly non-linear character of curve squeal. Remarkable in  
 414 the case  $\Delta y^{\text{WR}} = -10$  mm is the shape of the contact zone, which is split into three separate zones (Fig. 30).

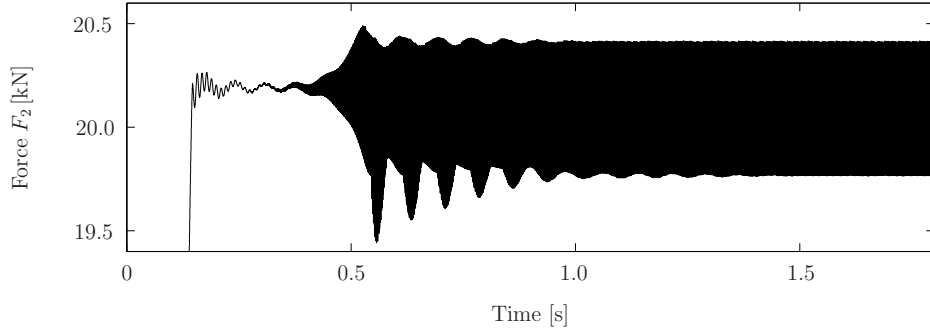


Fig. 27. Simulation XIII: time series of the lateral contact force  $F_2$ .

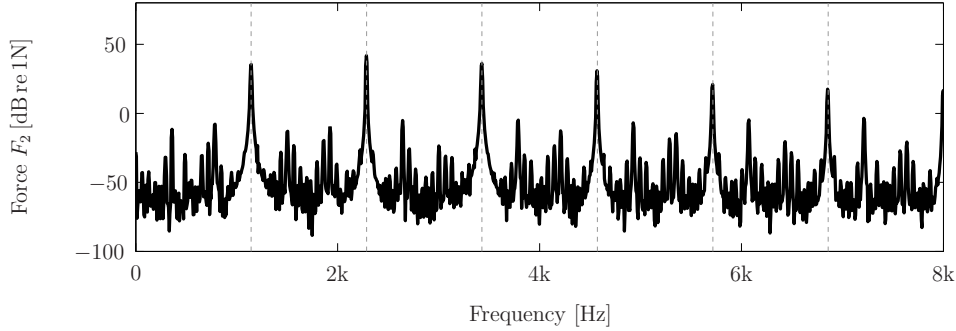


Fig. 28. Simulation XIII: power spectrum of the lateral contact force  $F_2$ . Multiples of the main frequency component at 1146 Hz are indicated by vertical dashed lines.

### 416 3.3 Discussion

417 The presented simulation results confirm that stick/slip during curving (and  
 418 consequently curve squeal) is possible not only in the case of a falling friction

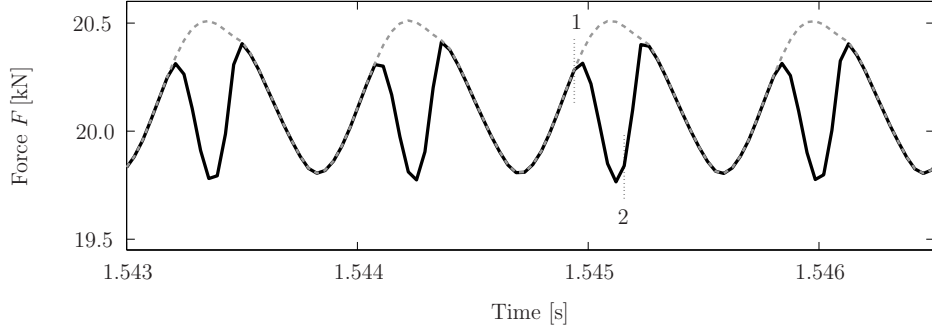


Fig. 29. Simulation XIII: zoom on time series of the contact forces; — lateral force  $F_2$ , - - - (grey) traction bound  $\mu F_3$ . The division of the contact zone at the time steps marked with Arabic numerals is depicted in Fig. 30.

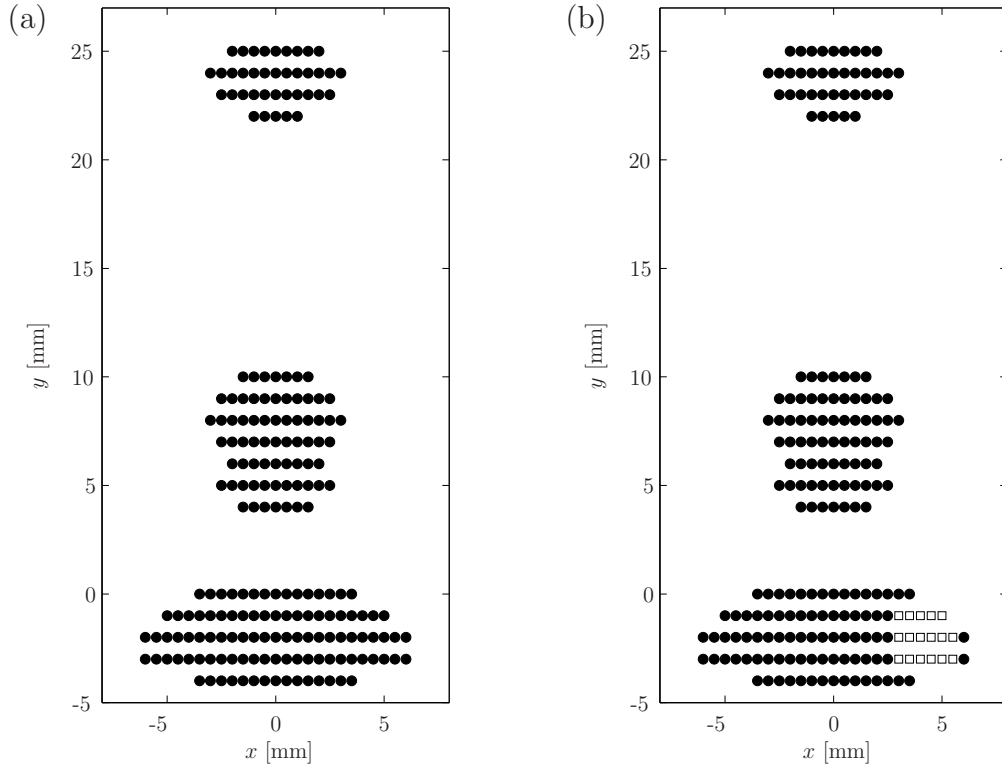


Fig. 30. Simulation XIII: division of contact zone in stick (□) and slip (●) zones; (a) minimum size of the stick zone (full slip corresponding to time step 1 in Fig. 29) and (b) maximum size of the stick zone (corresponding to time step 2 in Fig. 29).

419 coefficient, but also in the case of constant friction. The occurrence of stick/slip  
 420 is attributed to the coupling between vertical and tangential dynamics. The  
 421 time-domain simulations, however, give only limited insight into the precise  
 422 underlying mechanism. In the case of stick/slip at 5235 Hz, two wheel modes,  
 423 the axial (7,0,a) mode and the circumferential (2,c) mode, could be shown to

participate. If any of the two modes is assigned a very high modal damping ratio (e.g. 1), the stick/slip oscillation ceases to exist. For stick/slip at 434 Hz and 1146 Hz, only one mode could be shown to participate in each case, which is respectively the (2,0,a) axial mode and the (3,0,a) axial mode. In these two cases, the elimination of neighbouring modes from the frequency response function of the wheel did not have any influence on the stick/slip oscillation.

The validity of the simulations presented is limited by the model assumptions. The surface roughness of wheel and rail (which could be included as described in Section 2.4) and the slight inclination of the contact plane have not been considered. Both simplifications could influence the occurrence of stick/slip oscillations. It has been assumed that the lateral creepage and the lateral contact position do not change during the simulation, which is a reasonable assumption for quasi-static curving only. Furthermore, the friction coefficient was assumed to remain constant along the track, which is a questionable assumption for real conditions.

The simulation results are, however, in good qualitative agreement with general observations about squeal noise and results reported in the literature. Squeal is known to occur predominantly at frequencies corresponding to axial modes of the wheel with zero nodal circles ( $m = 0$ ) [1], which agrees with what is found here. The parameters investigated - the lateral creepage, the lateral contact position and the frictional properties - are key parameters for the occurrence of curve squeal [1,37] and they show a significant influence on the simulation results presented. de Beer et al. [8] found in a laboratory test that squeal occurs only above a threshold value of the angle of attack (i.e. the lateral creepage). This behaviour is clearly reflected in the results of Fig. 21. Based on the model of de Beer [8], Thompson [1] reports that squeal is most likely to occur if the contact on the wheel tread occurs towards the field side of the tread. The same result is seen in Fig. 26. Finally the results from Fig. 21, where pronounced stick/slip does not occur below friction values of 0.3, also agree with the well-known fact that low friction conditions (wet weather, lubrication) reduce the likelihood of squeal.

## 4 Conclusions

In this paper, a detailed time-domain model for the dynamic wheel/rail interaction was proposed. In order to keep computational effort in the wheel/rail interaction model as low as possible, vehicle and track were represented by impulse response functions derived from detailed FE models, which are calculated in advance. As contact model a transient, three-dimensional and non-linear contact model has been implemented based on Kalker's theory.

The implementation of the contact model has been validated for quasi-static

463 conditions against Kalker’s implementation CONTACT and showed very good  
464 agreement.

465 One essential feature of the simulation model is that the coupling between nor-  
466 mal and tangential directions is taken into account. This was a main condition  
467 for being able to investigate the occurrence of squeal for constant friction val-  
468 ues instead of falling friction curves.

469 In the rather limited parameter study presented in this paper, certain cases  
470 could be identified where strong unstable tangential contact forces appeared.  
471 In all cases, the exhibiting frequencies were close to wheel resonances corre-  
472 sponding to axial modes of the wheel with zero nodal circles ( $m = 0$ ). In  
473 this study, the lateral creepage, the lateral contact position and the frictional  
474 properties proved to be key parameters for the occurrence of curve squeal. In  
475 general, it was found that the conditions prevailing at the leading inner wheel  
476 (underradial position, contact towards field side of tread) promote squeal. All  
477 these findings are in good qualitative agreement with previously published  
478 findings on curve squeal.

479 In addition, the simulation results show that squeal can be observed even for  
480 a constant friction coefficient as suggested by previous publications.

481 Although the results shown in this paper are samples rather than due to an  
482 exhaustive parameter study, the results are promising and suggest that the  
483 model might be a good tool for carrying out well-controlled numerical ex-  
484 periments in order to increase the understanding of the mechanisms behind  
485 curve squeal. Especially noteworthy is that the model allows more realistic  
486 simulations taking into account the roughness of the wheel and rail running  
487 surfaces. However, for simulating real situations and perhaps even using such  
488 cases for validation, a better knowledge of the friction characteristics in the  
489 field is needed.

## 490 Acknowledgements

491 This work was performed as part of the activities within the Centre of Excel-  
492 lence CHARMEC (CHAlmers Railway MEChanics). I am grateful for advice  
493 and help by Prof. Wolfgang Kropp (CHARMEC, Chalmers University of Tech-  
494 nology) with the development of the wheel/rail interaction model. I would like  
495 to thank Prof. David Thompson (ISVR, University of Southampton) and Dr.  
496 Briony Croft (former PhD student at ISVR) for supplying me with the wheel  
497 model used in this paper. Furthermore, the access to the Wave Guide Fi-  
498 nite Element toolbox WANDS (developed by the Dynamics Group at ISVR),  
499 which I used for the modelling of the track, is greatly acknowledged. Finally, I  
500 would like to thank Dr. Peter Torstensson (CHARMEC, Chalmers University  
501 of Technology) for carrying out the GENSYS calculations.

## 502 References

- 503 [1] D. Thompson, *Railway Noise and Vibration: Mechanisms, Modelling and Means*  
504 *of Control*, Elsevier, Oxford, UK, 2009.
- 505 [2] M.J. Rudd, Wheel/rail noise - part II: Wheel squeal, *Journal of Sound and*  
506 *Vibration* 46 (3) (1976) 381-394.
- 507 [3] H. Stappenbeck, Das Kurvengeräusch der Straßenbahn - Möglichkeiten zu  
508 seiner Unterdrückung (The curve noise of the tramway - possibilities of its  
509 suppression), *VDI Zeitschrift*, 96 (6) (1954) 171-175.
- 510 [4] U. Fingberg, A model for wheel-rail squealing noise, *Journal of Sound and*  
511 *Vibration*, 143 (1990) 365-377.
- 512 [5] F. J. Périard, Wheel-Rail Noise Generation: Curve squealing by trams, PhD  
513 thesis, TU Delft, 1998.
- 514 [6] M.A. Heckl, I.D. Abrahams, Curve squeal of train wheels, part 1: Mathematical  
515 model for its generation, *Journal of Sound and Vibration* 229 (3) (2000) 669-  
516 693.
- 517 [7] M.A. Heckl, Curve squeal of train wheels, part 2: Which wheel modes are prone  
518 to squeal? *Journal of Sound and Vibration* 229 (3) (2000) 695-707.
- 519 [8] F.G. de Beer, M.H.A. Janssens, P.P. Kooijman, Squeal noise of rail-bound  
520 vehicles influenced by lateral contact position. *Journal of Sound and Vibration*  
521 267 (2003) 497-507.
- 522 [9] O. Chiello, J.-B. Ayasse, N. Vincent, J.-R. Koch, Curve squeal of urban rolling  
523 stock - part 3: Theoretical model, *Journal of Sound and Vibration* 293 (2006)  
524 710-727.
- 525 [10] J.F. Brunel, P. Dufrénoy, M. Naït, J.L. Muñoz, and F. Demilly, Transient model  
526 for curve squeal noise, *Journal of Sound and Vibration* 293 (2006) 758-765.
- 527 [11] G. Xie, P.D. Allen, S.D. Iwnicki, A. Alonso, D.J. Thompson, C.J.C. Jones, Z.Y.  
528 Huang, Introduction of falling friction coefficients into curving calculations for  
529 studying curve squeal noise, *Vehicle System Dynamics* 44 (Supplement) (2006)  
530 261-271.
- 531 [12] P.J. Remington, Wheel/rail squeal and impact noise: What do we know? What  
532 don't we know? Where do we go from here?, *Journal of Sound and Vibration*  
533 116 (2) (1985) 339-353.
- 534 [13] W. Lang, G. Roth, Optimale Kraftschlußausnutzung bei Hochleistungs-  
535 Schienenfahrzeugen (Optimal utilisation of adhesion for high-performance rail  
536 vehicles), *Eisenbahntechnische Rundschau* 42 (1993) 61-66.
- 537 [14] O. Polach, Creep forces in simulations of traction vehicles running on adhesion  
538 limit, *Wear* 258 (2005) 992-1000.

- 539 [15] A.D. Monk-Steel, D.J. Thompson, F.G. de Beer, M.H.A. Janssens, An  
540 investigation into the influence of longitudinal creepage on railway squeal noise  
541 due to lateral creepage, *Journal of Sound and Vibration* 293 (2006) 766-776.
- 542 [16] X. Liu, Meehan P.A., Investigation of the effect of lateral adhesion and rolling  
543 speed on wheel squeal noise, *Proceedings of the Institution of Mechanical*  
544 *Engineers, Part F: Journal of Rail and Rapid Transit* 227(5) (2013) 469-480.
- 545 [17] J.T. Oden and J.A.C. Martins, Models and computational methods for dynamic  
546 friction phenomena, *Computer Methods in Applied Mechanics and Engineering*  
547 52 (1985) 527-634.
- 548 [18] N. Hoffmann, M. Fischer, R. Allgaier, L. Gaul, A minimal model for studying  
549 properties of the mode-coupling type instability in friction induced oscillations,  
550 *Mechanics Research Communications* 29 (2002) 197-205.
- 551 [19] Ch. Glocker, E. Cataldi-Spinola, R.I. Leine, Curve squealing of trains:  
552 Measurement, modelling and simulation, *Journal of Sound and Vibration* 324  
553 (2009) 365-386.
- 554 [20] Y. Ben Othman, Kurvenquietschen: Untersuchung des Quietschvorgangs und  
555 Wege der Minderung (Curve squeal: Investigation of the squeal process and  
556 ways of mitigation), PhD thesis, TU Berlin, 2009.
- 557 [21] J.R. Koch, N. Vincent, H. Chollet, O. Chiello, Curve squeal of urban rolling  
558 stock - part 2: Parametric study on a 1/4 scale test rig. *Journal of Sound and*  
559 *Vibration* 293 (2006) 701-709.
- 560 [22] J. Jiang, D. Anderson, R.Dwight, The mechanisms of curve squeal, *Proceedings*  
561 *of the 11th International Workshop on Railway Noise (IWRN 11)*, pp.655-662,  
562 September 9-13, 2013, Uddevalla, Sweden.
- 563 [23] Z.Y. Huang, D.J. Thompson, C.J.C. Jones, Squeal prediction for a bogied  
564 vehicle in a curve, in: B. Schulte-Werning et al. (Eds.), *Noise and Vibration*  
565 *Mitigation for Rail Transportation Systems*, NNFM 99, Springer-Verlag, Berlin,  
566 Heidelberg, 2008, pp. 313-319.
- 567 [24] J.J. Kalker, A fast algorithm for the simplified theory of rolling contact, *Vehicle*  
568 *System Dynamics*, 11 (1982) 1-13.
- 569 [25] F. Wullens, W. Kropp, A three dimensional contact model for tyre/road  
570 interaction in rolling conditions, *Acta Acustica united with Acustica*, 90 (4)  
571 (2004) 702-711.
- 572 [26] A. Pieringer, W. Kropp, D.J. Thompson, Investigation of the dynamic contact  
573 filter effect in vertical wheel/rail interaction using a 2D and a 3D non-Hertzian  
574 contact model, *Wear* 271 (1-2) (2010) 328-338.
- 575 [27] A. Pieringer, W. Kropp, A time-domain model for coupled vertical and  
576 tangential wheel/rail interaction - a contribution to the modelling of curve  
577 squeal, in: T. Maeda et al. (Eds.), *Noise and Vibration Mitigation for Rail*  
578 *Transportation Systems*, NNFM 118, Springer, 2012, pp.221-229.

- 579 [28] A. Pieringer, Time-domain modelling of high-frequency wheel/rail interaction,  
580 PhD thesis, Chalmers University of Technology, Göteborg, Sweden, 2011.
- 581 [29] C.-M. Nilsson, C.J.C. Jones, D.J. Thompson, J. Ryue, A waveguide finite  
582 element and boundary element approach to calculating the sound radiated by  
583 railway and tram rails, *Journal of Sound and Vibration* 321 (2009) 813-836.
- 584 [30] A. Nordborg, Wheel/rail noise generation due to nonlinear effects and  
585 parametric excitation, *Journal of the Acoustical Society of America* 111 (4)  
586 (2002) 1772-1781.
- 587 [31] P.T. Torstensson, J.C.O. Nielsen, Monitoring of rail corrugation growth due to  
588 irregular wear on a railway metro curve. *Wear* 267 (2009) 556-561).
- 589 [32] DEsolver, GENSYs users manual, 2009.
- 590 [33] J.J. Kalker, *Three-Dimensional Elastic Bodies in Rolling Contact*, Kluwer  
591 Academic Publishers, Dordrecht, Boston, London, 1990.
- 592 [34] E. Andersson, M. Berg, S. Stichel, Rail Vehicle Dynamics, Lecture Notes, KTH  
593 Stockholm, 2007.
- 594 [35] E.A.H. Vollebregt, User' s Guide for CONTACT, J.J. Kalker's variational  
595 contact model, Technical Report, TR09\_03, version 0.9, VORtech Computing,  
596 Delft, The Netherlands, 2009.
- 597 [36] E.A.H. Vollebregt, A Gauss-Seidel type solver for special convex programs, with  
598 application to frictional contact mechanics, *Journal for Optimization Theory*  
599 *and Applications*, 87 (1) (1995) 47-67.
- 600 [37] N. Vincent, J.R. Koch, H. Chollet, J.Y. Guerder, Curve squeal of urban rolling  
601 stock - part 1: State of the art and field measurements, *Journal of Sound and*  
602 *Vibration* 293 (2006) 691-700.